Precision Engineering 97 (2026) 235–248

Contents lists available at ScienceDirect

Precision Engineering

journal homepage: www.elsevier.com/locate/precision

Defect analysis by computed tomography in metallic materials: Optimisation, uncertainty quantification and classification

Emanuele Avoledo [a,*], Marco Petruzzi [b], Marco Pelegatti [a], Alessandro Tognan [a], Francesco De Bona [a], Michele Pressacco [b], Riccardo Toninato [b], Enrico Salvati [a]

[a] Polytechnic Department of Engineering and Architecture, University of Udine, Via delle Scienze 206, Udine, 33100, Italy

[b] Lima Corporate Spa (a Company of the Enovis Group), Via Nazionale 52, Villanova, San Daniele del Friuli, 33038, Italy

ARTICLE INFO

Keywords:
Computed tomography
Additive manufacturing
Titanium alloy
Uncertainty quantification
Defect classification

ABSTRACT

This paper presents a methodology to optimise post-processing parameters in X-ray Computed Tomography (CT) for defect detection in metallic materials. The approach addresses three main goals: minimisation of systematic errors in defect reconstruction, quantification of uncertainty, and reliable defect classification. The proposed methodology aims to remove the systematic error that impacts defect reconstruction, thereby improving the accuracy of defect size and morphology assessment, which is essential for fatigue life prediction, particularly in materials produced through additive manufacturing (AM). An iterative comparison between CT-based defect and fractographic measurements is involved to identify the optimal CT post-processing parameters, such as the grey threshold (GT). The methodology was applied to 11 dog-bone-shaped titanium alloy samples (5.5 mm nominal gauge diameter) produced via electron beam melting. The optimisation procedure resulted in a GT value that was 134% of that obtained using a commercial algorithm, effectively removing the systematic uncertainty associated with Murakami's parameter $\sqrt{area}$. The uncertainty of various defect features, such as equivalent diameter, sphericity and aspect ratio, was calculated by propagating the remaining stochastic uncertainty of $\sqrt{area}$. An unsupervised K-means algorithm categorised unlabelled defects into three major types often encountered in AM: gas pores, keyholes, and lack of fusion. Finally, the labelled defects were processed through a support vector machine to infer the analytical form of the decision boundaries, achieving an accuracy of 99%.

1. Introduction

The presence of manufacturing defects in structures typically reduces the mechanical properties and leads to unexpected collapses. Focusing on fatigue scenarios, internal defects and surface irregularities act as stress raisers and constitute possible candidates for crack nucleation sites [1,2]. In particular, this phenomenon is especially critical for metallic components fabricated through additive manufacturing (AM) powder-based processes. In recent years, metal AM has been used to produce final end-use parts in different industrial fields, e.g. aerospace [3], automotive [4], and medical [5]. Despite the undeniable advantages given by AM, e.g. structural complexity and topology optimisation [6], this manufacturing process notoriously introduces the formation of peculiar defects, such as lack of fusion (LOFs), gas pores (GPs) and key holes (KHs) [7].

These three categories of defects exhibit distinct origins and morphologies, which are determined by different process parameters. GPs are characterised by small size and a regular spherical shape. KHs are the largest of the defects and retain a spherical shape. The formation mechanisms of these two defect types differ significantly. GPs are caused by gas molecules trapped in the melting pool, often present in the powder due to gas entrapment during raw material atomisation. In contrast, KH defects stem from excessive localised heat input [8]. In contrast, LOF defects show an irregular, plane-elongated shape perpendicular to the build direction and large dimensions, i.e. they generally exhibit a low aspect ratio [9]. LOF defects are usually the most detrimental concerning fatigue performance. They occur when the laser's heat is insufficient to fully melt the metal powder, leading to poor adhesion between the top layer of powder and the layer beneath and inadequate overlap of laser tracks. Additionally, LOF defects can arise from poor powder distribution within the specific layer [10,11].

The relationship between different defect types and fatigue life has been widely studied but is currently the subject of debate [12]. The standard semi-empirical models, like those belonging to the Linear Elastic Fracture Mechanic (LEFM) theory, approximate defects as cracks

* Corresponding author.
E-mail addresses: avoledo.emanuele@spes.uniud.it (E. Avoledo), enrico.salvati@uniud.it (E. Salvati).

https://doi.org/10.1016/j.precisioneng.2025.09.008
Received 18 November 2024; Received in revised form 27 August 2025; Accepted 8 September 2025
Available online 20 September 2025

with a characteristic length equal to the square root of the defect surface projected on the plane orthogonal to the loading direction, referred to as $\sqrt{area}$ [13]. In this model, the distance between a defect and the free surface of the sample and $\sqrt{area}$ are the only defect features considered to compute the Stress Intensity Factor (SIF). Recently, several machine learning (ML) models have been developed to predict with remarkable accuracy the fatigue life based on databases containing information about both the dimension and morphology of defects [14–19].

Classification of defect types present in the material guides the selection of process parameters to minimise defect presence [20–22] and is also becoming fundamental for making accurate predictions about mechanical properties. Recently, ML algorithms have been implemented to achieve defect classification. For example, Snell et al. demonstrated the superior accuracy of an unsupervised ML algorithm compared to a defined limit method for clustering defects based on 3D pore data [23]. Poudel et al. proposed two ML algorithms for the classification, i.e. a decision tree and an artificial neural network, based on nine different parameters describing defects' dimension and morphology. The two algorithms reached an accuracy higher than 98% [24]. Furthermore, Minerva et al. performed a classification algorithm to detect pores, pore clusters and LOFs to enhance the ability of the extreme value statistic (EVS) in predicting the maximum defect size [25].

The defect characteristics are typically characterised by X-ray micro-computed tomography (CT). This non-destructive inspection technique allows the reconstruction of the whole morphology of the internal defects [26,27]. Defects attenuate the intensity of the emitted X-rays after penetrating the gauge volume, while a detector collects the X-rays. The attenuation data are quantified through a prescribed grey threshold (GT) and post-processed to generate a set of digital images of volume sections. The images are circularly stacked, and the 3D reconstruction is realised [28]. A pixel represents the elementary unit of an image, characterised by a specific level of grey, while its three-dimensional extension is referred to as a voxel. Image segmentation is the process of differentiating between the voxels of the material and those of the background. Many different algorithms can be used to segment an image or volume, including global and local thresholding, edge detection, statistical shape models and deep convolutional neural networks [29–31].

Throughout the process, from data acquisition to reconstruction of the internal defects, various sources of uncertainties affect the final measurements, such as spatial resolution, user-defined parameters, surface determination, composition and size of the scanned object and temperature [32]. Overall, the error committed in defect surface determination is recognised as one of the most impactful errors [33], and the elaboration of an algorithm to improve the accuracy of surface determination is an active research topic [34].

Several approaches have been proposed to address uncertainty evaluation in CT-based defect measurement. One standard method is to use a reference sample with a known porosity distribution to estimate the error introduced by the CT scan. This approach is known as the substitution method. The critical point of this method is that the reference object must be comparable in shape, dimensions and material to the test sample [35–37]. Metallographic observations of multiple sample sections analysed by CT scan provide a commonly used reference porosity measurement. The metallographic analysis can be used to calculate a reference value of the porosity of the sample to compare with that estimated by the CT scans, as in [38]. Alternatively, the metallographic-based reference value can be used to directly compare the dimensions of the detected defects with both techniques, as demonstrated in [39].

This paper presents a novel method for optimising defect detection in CT scans, which involves identifying and eliminating systematic errors. Consequently, the remaining uncertainty is limited to the stochastic error. A case study is presented to demonstrate the capabilities of the developed framework analysing the CT defect reconstruction of a set of 11 Ti6Al4V samples produced using the electron beam melting (EBM) technique. Since the nature of the defects is not known a priori, the dataset is classified by K-means, so the defects are categorised into GP, KH and LOF based on the appropriate constraints on shape and morphology. Subsequently, labelled defects are processed using a support vector machine (SVM) to determine the approximate analytical form of the decision boundaries.

The objective of this paper is threefold. Firstly, a novel methodology is presented for optimising the CT process parameters to reduce the systematic error committed to measuring $\sqrt{area}$. Secondly, the uncertainty quantification based on the residual stochastic error of $\sqrt{area}$ is achieved for some defect features measured indirectly. Lastly, for the defect clustering, a K-means algorithm is performed based on the values of $\sqrt{area}$, sphericity and aspect ratio of all defects. The boundaries of the three defect clusters (GP, KH and LOF) are identified by applying a supervised machine learning (ML) algorithm, the Support Vector Machine (SVM) algorithm.

2. Proposed approach

2.1. CT-based defect analysis optimisation

The key idea of the proposed algorithm is to improve the accuracy of CT-based defect characterisation by comparing segmented defect sizes with reference measurements obtained through post-mortem fractographic analysis. The fractographic analyses were conducted after the samples had undergone high cycle fatigue failure. The high cycle fatigue tests were performed close to the material's fatigue limit, ensuring that the fatigue crack propagation rate was sufficiently low to minimise plastic deformation. In this research, each defect is regarded as a crack with a length equal to Murakami's parameter, $\sqrt{area}$.

Proper alignment between the fractographies and the CT reconstruction is essential to identify the defects that are traversed by the fracture surface. To achieve this, bespoke markers were first affixed to the samples as a reference point for the alignment before performing the CT scan. Next, high-cycle fatigue tests were performed, after which the geometry of the fractured sample halves was obtained using a 3D laser scanner. Finally, the CT defects, laser reconstruction of the two sample halves and the fractography images were aligned using the bespoke markers and the fracture surface. Following the alignment process, CT- and fractography-based measures of $\sqrt{area}$ were determined for the CT defects corresponding to those observed on the fractographies. This procedure enables a direct comparison of the dimensions of the CT defects with the actual defects, thus facilitating investigation into the relationships between the parameters that guide the CT scan defect analysis and the accuracy of the outcomes.

The first stage of the optimisation framework involves quantifying the error, E, related to the discrepancy of $\sqrt{area}$ estimated by CT and fractography:

$$E_{\sqrt{area}} = \sqrt{area}_F - \sqrt{area}_{CT}, \tag{1}$$

where $\sqrt{area}_F$ and $\sqrt{area}_{CT}$ are respectively the fractography and CT measurements of $\sqrt{area}$. Note that $E_{\sqrt{area}}$ in Eq. (2) represents the sum of the systematic, $\Delta_{\sqrt{area}}$ and stochastic, $u_{\sqrt{area}}$ errors:

$$E_{\sqrt{area}} = \Delta_{\sqrt{area}} + u_{\sqrt{area}}. \tag{2}$$

If $E_{\sqrt{area}}$ exhibits a Gaussian distribution, the definitions of systematic and stochastic errors can be expressed as follows:

$$u_{\sqrt{area}} = k \cdot s_{E_{\sqrt{area}}}, \tag{3}$$

$$\Delta_{\sqrt{area}} = \overline{E}_{\sqrt{area}}, \tag{4}$$

where $s_{E_{\sqrt{area}}}$ and $\overline{E}_{\sqrt{area}}$ represent the standard deviation and the median or mean value of the distribution of $E_{\sqrt{area}}$, while k is the tolerance interval factor [40].

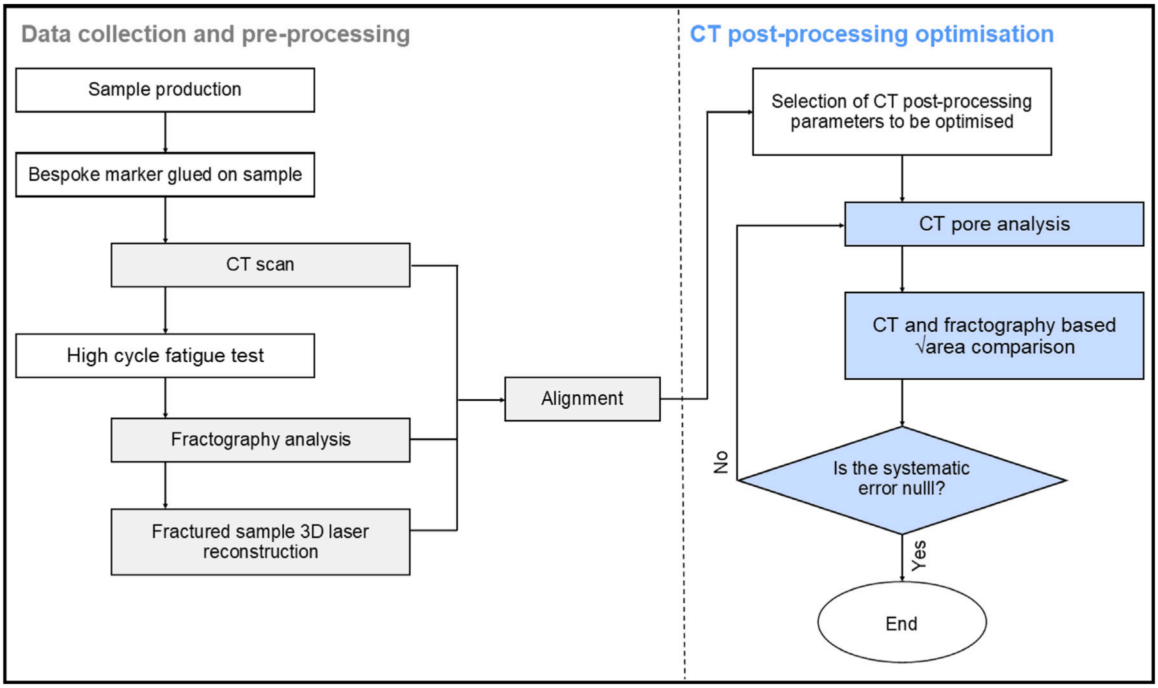

Fig. 1. Block diagrams of the procedure followed in selecting the optimised CT defect analysis parameters and estimating the defect features' uncertainty.

Once the set of CT parameters to be optimised has been defined, the CT defect analysis must be performed multiple times using different parameter values. A region of interest (ROI) can be selected to apply the defect reconstruction algorithm specifically to the gauge volume of the sample. Before starting with the iterative optimisation process, the geometry of the samples acquired with the 3D laser and the ROI used in defect detection must be aligned with the fractography results. The 3D laser reconstruction and ROI alignment is guided by a marker attached to the sample surface. At the same time, the fractography aligns with the fracture surface identified at the interface between the laser reconstructions of the two sample halves.

After each iteration, the extraction of reference defects is based on the alignment between fractographies and CT results. The application of Eq. (1) provides guidance on adjusting the parameter values to minimise systematic errors and stochastic variations.

The optimisation method presented in this paper can be adopted with any segmentation algorithm that requires a parameter selection and is not restricted to the algorithm considered in this work. The whole procedure is summarised in Fig. 1.

2.2. Defect descriptor uncertainty quantification

Once the optimal defect analysis parameters have been identified, assessing the uncertainty associated with all defect features with an analytical expression using Error Propagation Theory (EPT) becomes possible. While the defect dataset for the CT optimisation included only those defects reconstructed by the CT and also present in the fractographies, the uncertainties can be propagated for all the defects detected by the CT analysis. The first step is to determine the prediction interval for $\sqrt{\text{area}}$ whose boundaries correspond to the associated stochastic uncertainty, denoted as $u_{\sqrt{\text{area}}}$. Since a Gaussian distribution is assumed for $E_{\sqrt{\text{area}}}$, the tolerance interval of $\sqrt{\text{area}}$ can be expressed as:

$$\sqrt{\text{area}} \in [\sqrt{\text{area}}_{CT} - u_{\sqrt{\text{area}}}, \sqrt{\text{area}}_{CT} + u_{\sqrt{\text{area}}}], \tag{5}$$

After determining $u_{\sqrt{\text{area}}}$, a straightforward procedure can be applied to evaluate the uncertainty associated with other defect characteristics based on this quantity. An example is provided in Appendix, where the uncertainties of both specific CT-based measurements and the defect features derived from them are determined by applying EPT. In the case study, the main formulas are recalled and applied. According to [41], all sources of uncertainty should be treated in the same way. Therefore, if a systematic error persists at the end of the optimisation process, it can be propagated, adopting the same procedure used for stochastic uncertainty, through the derived quantities and subsequently removed to adjust the final values accordingly.

2.3. Defects classification

An unsupervised ML algorithm was used to identify the conditions that must be met to categorise defects correctly. This type of algorithm autonomously infers patterns in unlabelled data. A K-means algorithm is proposed for classifying defects. This algorithm analyses a dataset and determines the optimal way to divide it into K clusters. In this case, K is set to three to represent the main categories of defects, i.e. GP, KH and LOF. As the first step, the algorithm randomly selects the centroids of each cluster, assigning the closest defects to them. Then, the centroids' positions are refined by optimising a cost function, defined as the sum of squared distances between defects and their assigned centroids [42]. Once the K-Means algorithm labelled the defects, an SVM classifier (SVC) with linear kernel analytically determines the hyperplanes that optimally separate the clusters given by the previously executed K-Means [43].

3. Case study

A batch of 11 samples of Ti6Al4V powders were manufactured via Electron Beam Melting (EBM). The machine model was Q10Plus, distributed by Arcam EBM, equipped with EBMControl 5.2, 50 μm slicing was used to manufacture the specimens and custom process parameters (machine themes) for Ti6Al4V. Plasma atomised Ti6Al4V powder from AP&C, compliant to ISO 5832-3 [44] and custom specs, was used. The selection of the parameters governing the AM process was not the focus of the present study. The samples have the shape as per ASTM E466-15 [45] (generally used for fatigue characterisation purposes), and in Fig. 2, a detail of the gauge part is shown. All

Table 1
Technical specifications of Zeiss Metronom 1500 tomograph.

Technical parameter	Specification	Value
Radiogenic Tube	Max voltage Max electric current Max power	225 kV 3000 μA 225 W
Detector	Pixel number Pixel dimension	3072 × 3072 139 × 139 μm
Highest resolution		12 μm
Measuring range (max vertical extension of the image field)	Max diameter Max height	330 mm 270 mm
Measuring range (max horizontal extension of the image field)	Max diameter Max height	330 mm 870 mm
Max piece weight		50 kg

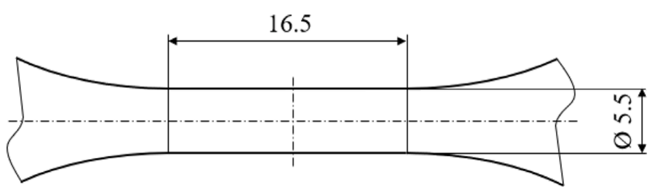

Fig. 2. Length and diameter of the gauge volume of samples in millimetres.

Table 2
Optimal acquisition parameters for CT scans.

Acquisition parameter	Value
Voxel dimensions	12 × 12 × 12 μm
Voltage	199 kV
Electric current	67 μA
Integration time	1000 ms
Gain	1
Image averaging	4 images
Binning	1 × 1
Number of projections	2250

Table 3
Summary of the tested parameters of the 12 cases considered for the uncertainty analyses.

GT	POD	MEA
100% DGT	0.0	Grid-based
110% DGT	0.5	Ray-based
130% DGT	-	-

samples were machined to reduce the surface roughness to focus the analysis on internal defects enucleation and facilitate defect analysis via non destructive techniques (surface irregularities are prone to enhance noise on the acquired data via CT [46]).

Section 3.1 illustrates the procedure adopted to acquire the CT data and the reference measurement by fractography. Subsequently, Section 3.2 outlines the selection of the case study optimal CT post-process parameters, which corresponds to GT, probability of detection (POD) and defect mesh extraction algorithm (MEA). Therefore, the CT-based measurement of $\sqrt{\text{area}}$ was depurated by the systematic error as well as the defect characteristics measurements, i.e. volume, surface area and axial projections. The stochastic uncertainty of all the considered defect features, i.e. equivalent diameter, sphericity and aspect ratio, is quantified through linear error propagation, given the stochastic uncertainty of $\sqrt{\text{area}}$ in Section 3.3. Finally, Section 3.4 describes the classification process based on K-means and SVC.

3.1. *Experimental dataset acquisition*

3.1.1. *X-ray CT scans and defect analysis*

Before scanning the sample, a bespoke reference marker was placed on the surface of the sample to facilitate the post-mortem correlation with the fractographic analysis and the laser reconstruction of the geometry of the fractured sample halves. Then, the samples were analysed by CT to characterise the material's morphological structure and, in particular, the internal defects. The CT scanner was a Zeiss Metronom 1500, and the corresponding technical specifications are reported in Table 1.

The parameters used for the CT analyses are shown in Table 2.

The software VGStudio Max® was employed for CT reconstruction and pore analyses, thus enabling the segmentation of empty volumes (pores or defects) from solid material. Specifically, the defect identification analysis was conducted by the VGEasyPore® algorithm based on a contrast level threshold. If the difference in grey intensity between a voxel and its closest neighbour exceeds the pre-defined contrast threshold, then the voxel is categorised as part of a defect. Fig. 3 shows an example of defect analysis results applied to one of the 11 samples analysed. In particular, Fig. 3a, b and c show three planar views of the sample, specifically with the z-axis oriented as the sample axis and the x and y axes orthogonal to the z-axis. Fig. 3d displays a view of all the defects detected within the selected region of interest.

Each group of voxels classified as potential defects is assigned a POD to determine whether it is a defect rather than a misrepresentation. The correct choice of GT and POD is essential for accurate defect detection. Regarding GT, the software initially suggests a default value corresponding to the threshold between the sample's surface and the surrounding air volume. This value serves as the initial condition and is then finely tuned to achieve the most accurate representation of the sample's internal structure, as will be shown later.

To optimise the defect detection algorithm, it was decided to perform the defect analysis with different values of the post-processing segmentation parameters, i.e. default grey threshold (DGT) and POD, to study their influence on the determination of the uncertainty of the defect size. The DGT proposed by the software was taken as a reference, and different percentages, such as 100%, 110% and 130%, were tested. For the POD, two thresholds were considered: 0.0 and 0.5. The present study covered all the possible combinations of the parameters listed in Table 3, totalling 12 cases.

The proposed methodology involves the 3D reconstruction of defects through a mesh extraction algorithm (MEA). The 3D defect reconstruction is necessary to identify which CT-scan-based defects correspond with the footprints observed on the fractographies, enabling the comparison of the corresponding $\sqrt{\text{area}}$. Notably, $\sqrt{\text{area}}$ is computed based on the 3D reconstruction rather than being directly extrapolated from the VGEasyPore analysis. Therefore, the MEA must be carefully selected to minimise its impact on defect sizes. VGStudio Max® implements two MEA: grid-based and ray-based. This case study tested both algorithms to prove their performance and analyse their accuracy. The

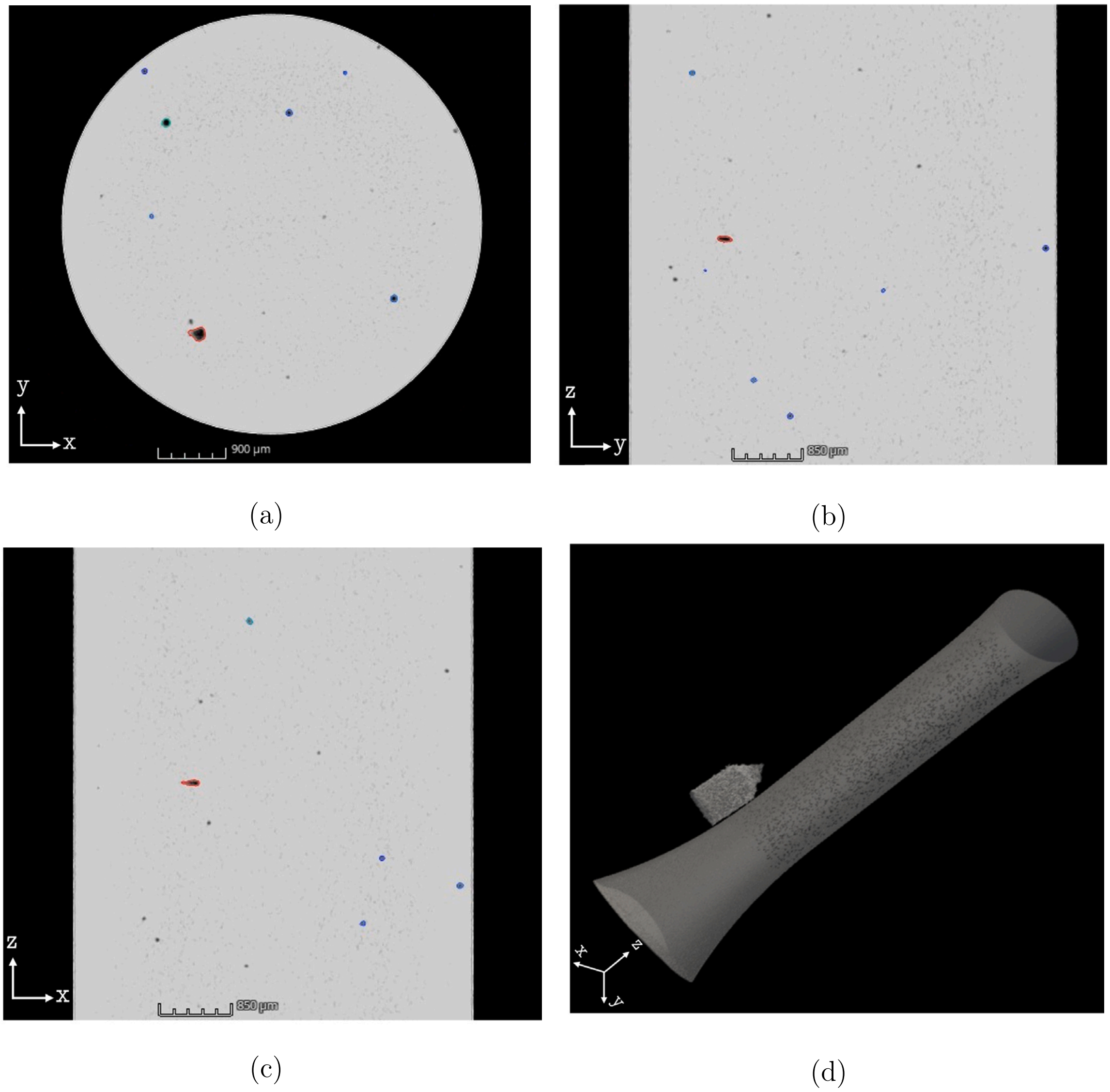

Fig. 3. Defect analysis result of one of the 11 case study samples. (a) Transversal section, plane x-y; (b) longitudinal section, plane y-z; (c) longitudinal section, plane x-z; (d) defects detected in the region of interest of the defect analysis.

grid-based algorithm involves dividing the whole space with a three-dimensional regular grid. Each element is analysed and associated with bulk material, defect, or transition zone based on the value of the grey intensity. The ray-based algorithm virtually scans the whole volume to analyse with rays. The borders of the defects are identified based on the grey values among the rays. Both algorithms must set a GT to separate the material and the void.

3.1.2. Fractography and 3D laser scan

After collecting the data required for reconstructing the internal structure of the sample, the next step is to measure the actual dimensions of the defects for comparison. To achieve this goal, all the samples were tested with a cyclic load near the fatigue limit of the material. In this way, the plastic deformation is negligible, and defects preserve their sizes. The study of material properties based on fatigue test results is beyond the scope of this paper. The material and the fracture surfaces were observed using a Scanning Electron Microscope.

The fracture surface is assumed to cross defects at the largest cross-section. This is a reasonable assumption because the SIF is higher in this section. LOF defects are typically flat and develop in a plane orthogonal to the building direction — the same plane in which fracture propagation occurs — which makes them the most detrimental to fatigue performance.

Aligning the fractographies with the CT sample reconstruction is essential to identify the defects observed in both the CT scans and fracture surfaces. To enable this alignment, the external geometry of the fractured parts was acquired using a 3D laser scan. The present research used the COMET L3D 8M 150 mm optical 3D measurement system, and the parameters adopted are given in Table 4, whereas a laser reconstruction of the fractured sample is depicted in Fig. 4.

3.1.3. Alignment of CT defects, fractography images and fractured sample

The measure of $\sqrt{area}$ is obtained from the fractographic analysis of the fracture surfaces. To compare the size of defects obtained through fractographic and CT analysis, a bespoke alignment method was developed.

The alignment was carried out in NX®, a 3D modelling environment capable of handling STL files. The first step is to import the volume reconstruction of one of the sample halves into the 3D environment to define the local Cartesian coordinate system. Specifically, the z-axis was oriented as the fatigue load direction, and the x- and y-axes were in the transverse plane found relative to the indentation of the sample clamping jaws. The local system was then aligned with the global

Table 4
Acquisition parameters for 3D laser scan and lens details.

Parameter	Value
Resolution [megapixel]	8.1
Working distance [mm]	760
Shortest measuring time [s]	1.7
Measuring volume [mm^3]	140 × 105 × 80
3D point spacing [μm]	42
Camera lens	STEINBICHLER - COMET - L3D - 8M 150 - 80.0mm - Camera
Projector lens	STEINBICHLER - COMET - L3D - 8M 150 - 50.0mm - Projector

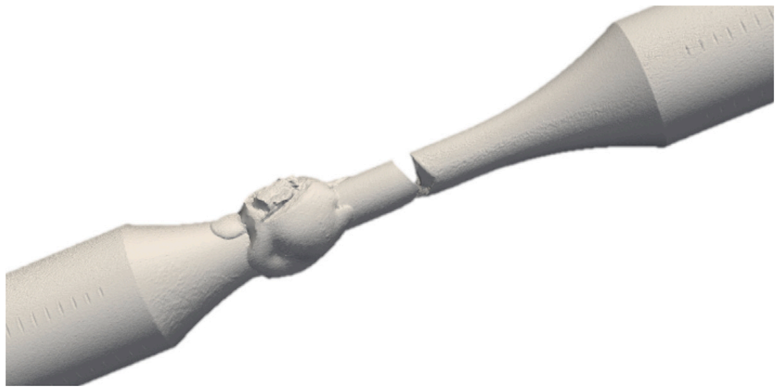

Fig. 4. 3D laser reconstruction of a fractured sample.

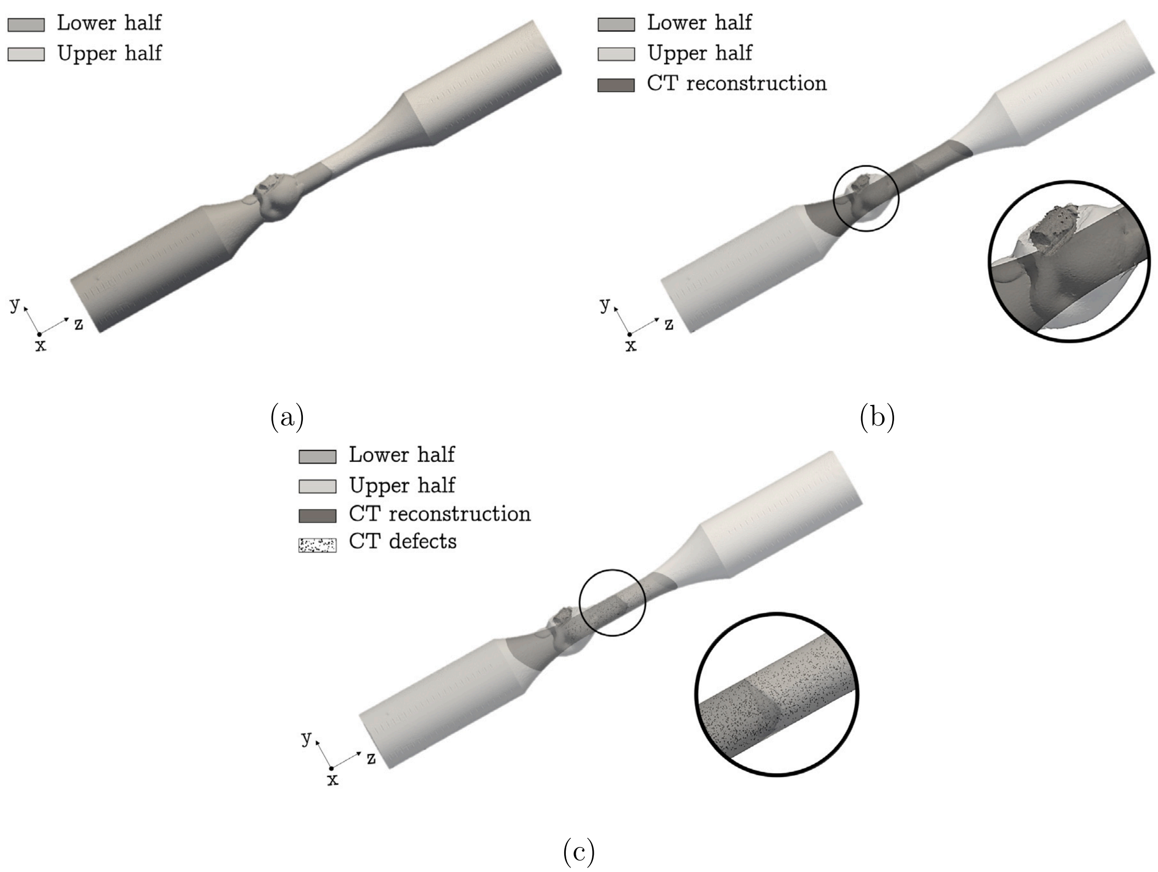

Fig. 5. Steps of the alignment between 3D laser reconstruction of sample's halves and CT reconstruction of the ROI and the corresponding internal defects. (a) Sample halves laser reconstruction, (b) overlapping of the sample volume fraction reconstructed with CT scan and a detail of the attached marker, (c) visualisation of the detected defects with VGEasyPore® within the ROI and a detail of the fracture area.

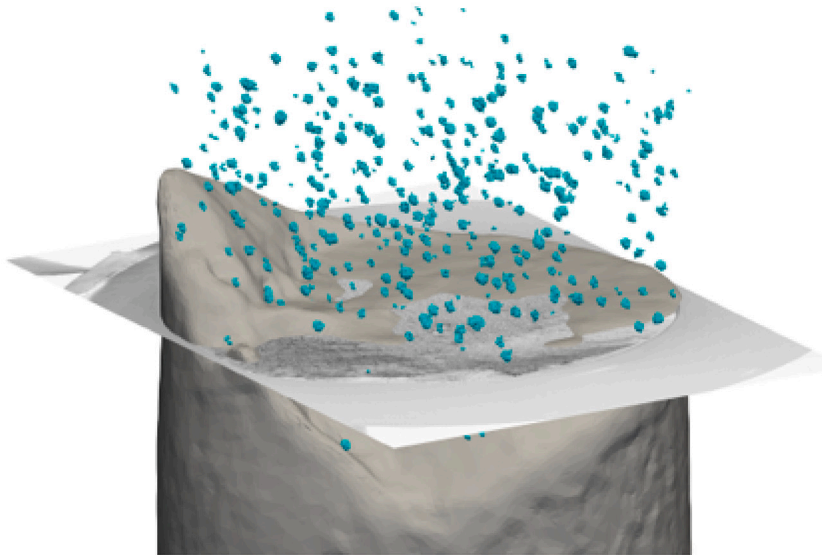

Fig. 6. Example of alignment between a fractured sample half, the fractography and the defects detected by VGEasyPore®.

coordinate system. The same procedure was carried out for the second half. In this way, both halves were aligned with the global coordinate system to reconstruct the entire shape of the selected specimen. Then, the mesh of the specimen's ROI, obtained with the CT scan, was manually aligned with the reconstructed shape, and the set of defects automatically followed this orientation. A marker glued to the sample surface before the CT scan facilitated the alignment between the laser and CT reconstructions of the sample volume. Fig. 5 shows the result of this process. In particular, the fracture surface and the presence of the marker can be observed.

The final step involved importing the fractography results (2D image) into the 3D modelling environment and then superimposing them on the fracture surface identified by one of the sample halves.

For instance, Fig. 6 depicts the result of this alignment process applied to a specimen. Specifically, the image shows the lower half, the fractography of the lower fracture surface and a portion of the CT defect cloud. The process was then applied to all specimens.

Fig. 7 shows a different view of the alignment result. It shows the fracture surface from above. The CT defects corresponding to those observed in the fractography are highlighted in red. It is worth observing that a few red defects lying within the monotonic static fracture surface (bottom-right) show some misalignment with the underlying fractographic identification. This is attributed to the inevitable plastic deformation involved in this area.

3.2. Experimental CT-based defect analysis optimisation

This section presents the details of the selection criteria for the optimum CT post-processing parameters. The defect dataset included the CT-detected defects that matched those shown within the fractography images of the 11 samples. The choice of the POD threshold affects solely the number, not the size, of the defects detected by the algorithm. Specifically, increasing the POD reduces the number of identified defects, as smaller defects are excluded. As the largest defects are typically the most damaging in machined specimens, a POD of 0.5 was considered acceptable, as it allowed for an accurate representation of the internal defects while filtering out small ones with negligible impact on fatigue life.

In terms of MEA selection, the ray-based algorithm resulted in fewer defects compared to the grid-based one, under the same conditions. Furthermore, while varying the POD from 0.0 to 0.5, the grid-based algorithm consistently preserved the defect shapes, whereas the ray-based algorithm did not. Given that POD should influence only the number of defects and not their dimensions, the grid-based algorithm was selected for its reliability in maintaining geometric consistency.

Table 5
Number of CT defects on the fractography surface, mean, median, and standard deviation of $E_{\sqrt{\text{area}}}$ for each analysed GT value.

GT [% of DGT]	N. of defects –	Mean [μm]	Median [μm]	St. dev. [μm]
100	80	−15.85	−12.35	14.90
110	80	−10.13	−8.41	12.36
130	73	−3.23	−1.27	10.87

Once the POD and the MEA were chosen, only the uncertainty associated with the GT selection had to be assessed. This objective was achieved by analysing $E_{\sqrt{\text{area}}}$ obtained with Eq. (1) for each of the different values of GT.

Fig. 8a compares all the scenarios with different GT settings with the fractography measurements. For confidentiality reasons, the values of $\sqrt{\text{area}}$ reported in the figure have been normalised by dividing each distribution by the median value of the distribution of $\sqrt{\text{area}}_F$. In Fig. 8a, the defects are sorted by size using the fractography measurements as a reference. As can be seen, the CT-evaluated $\sqrt{\text{area}}$ of the defects tends to decrease as the GT increases, in line with theoretical expectations. Fig. 8b shows the distributions of $E_{\sqrt{\text{area}}}$ obtained for each GT setting. The symmetry of the distribution allowed a Gaussian distribution to be assumed to approximate $E_{\sqrt{\text{area}}}$, which implies that the standard deviation, $s_{E_{\sqrt{\text{area}}}}$, can be directly correlated with the stochastic uncertainty of the experimental measurement of the defect cross-section according to Eq. (3).

Table 5 summarises the primary information associated with these distributions, i.e. the number of defects appearing in the fractographic and CT analysis, mean, median and standard deviation.

As GT increases, all the quantities reported in Table 5 decrease. The mean and the median are connected with the location of the distribution, which gets closer to zero. This is the goal of the optimisation process. The standard deviation and the stochastic uncertainty of $\sqrt{\text{area}}$ are connected by Eq. (3). This implies that a decrease in the standard deviation produces a decrease in the uncertainty and, therefore, an improvement in the accuracy. The decreasing number of detected defects is in line with the expectation because an increase in GT translates to a decrease in the defect dimensions, so the smallest defects may not be detected any more.

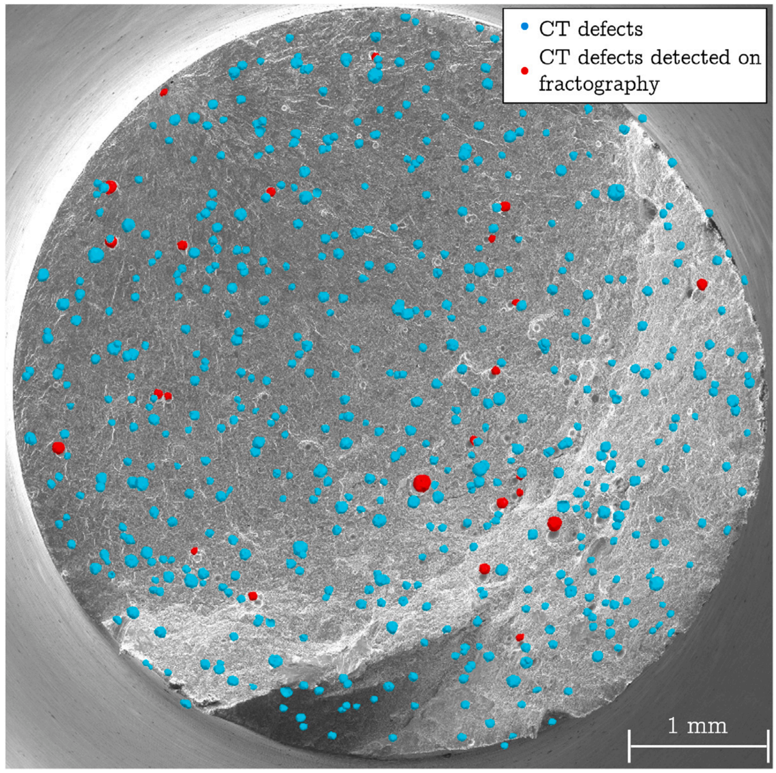

Fig. 7. Overlay of the fracture surface micrograph and the CT-based reconstructed defects.

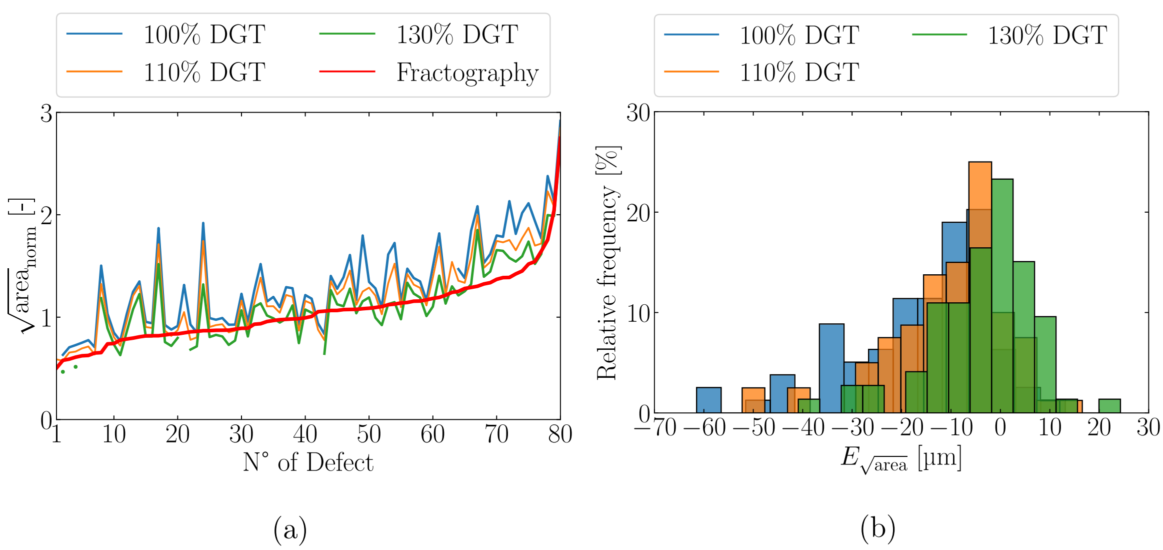

Fig. 8. (a) Comparison between the outcomes of the CT scans post-processing with different GT values and the fractography in terms of normalised $\sqrt{\text{area}}$; (b) Distribution of $E_{\sqrt{\text{area}}}$ for each GT setting.

Fig. 9 offers the graphical overview of the data in Table 5. Given the qualitative arrangement of each set of points, the data were fitted using ordinary least squares (OLD).

Finally, Table 6 details the optimal parameters settings that nullify the systematic error in measuring $\sqrt{\text{area}}$.

Table 6
Optimal setting for the considered defect analysis parameter.

Parameter	Optimal setting
GT	134% of GDT
POD	0.5 (50%)
MEA	Grid-based

3.3. Experimental defect descriptor uncertainty quantification

This section deals with the evaluation of the uncertainty associated with different defect descriptors, i.e. sphericity, aspect ratio and equivalent diameter, using EPT. The evaluation is based on the residual stochastic uncertainty related to the measurement of $\sqrt{\text{area}}_{\text{CT}}$ computed according to Eq. (3) and based on the distribution of $E_{\sqrt{\text{area}}}$.

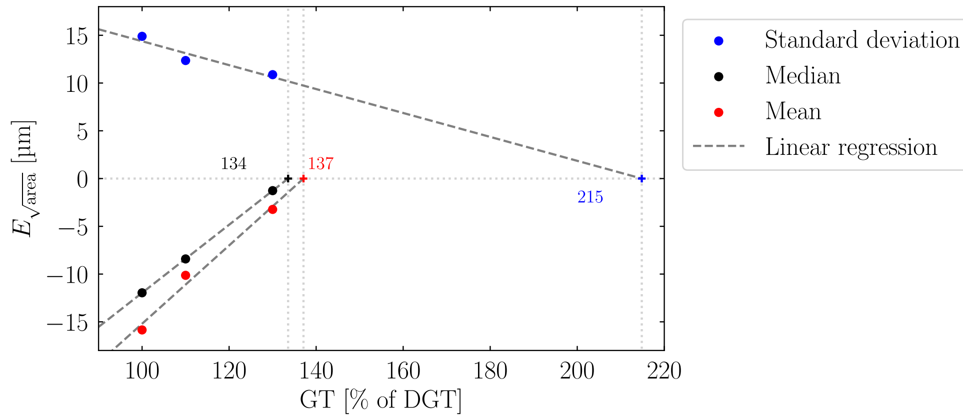

Fig. 9. Linear regression between the mean, median and standard deviation of $E_{\sqrt{\text{area}}}$ and GT values.

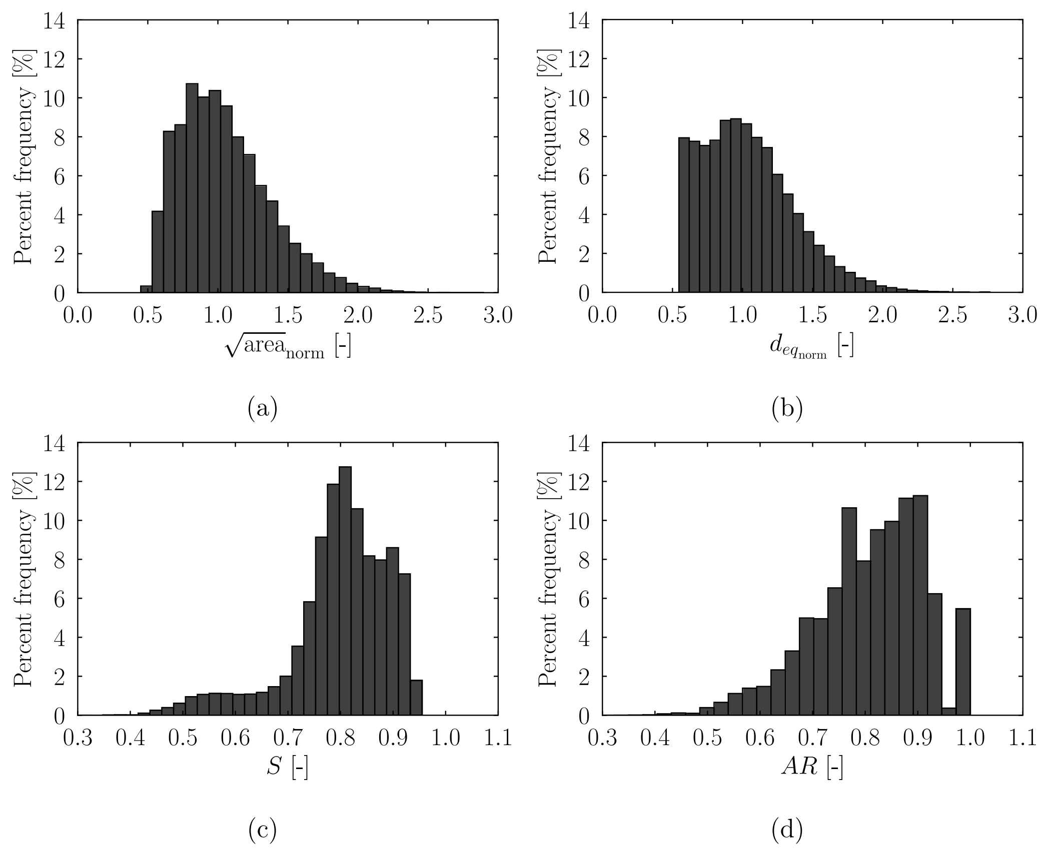

Fig. 10. Distributions of: (a) $\sqrt{\text{area}}$, (b) d_{eq}, (c) S and (d) AR.

At this point, the uncertainty analysis can be extended to the entire defect database formed by combining all the defects detected by the CT analyses for all 11 samples. All CT defect analyses were performed with a GT equal to 130% of the DGT and a POD of 0.5. The selection of the MEA was only involved in the determination of $u_{\sqrt{\text{area}}}$. The defect database, which is comprehensive of all the 11 samples involved in the CT optimisation, contains 28688 defects. Fig. 10 shows the distributions of the defect characteristics of the whole database. Note that again $\sqrt{\text{area}}$ has been normalised by dividing by the corresponding median value; the same normalisation is also applied to d_{eq}.

The most general approach involves correcting the defect descriptor values obtained from a non-optimal set of parameters to eliminate systematic error. Once this correction has been made, the remaining stochastic uncertainty can be evaluated. It is important to note that the correction step is unnecessary if the CT defect analysis is performed using optimal parameters. The process of value adjusting and error propagation is summarised in the following steps.

1. The values of $u_{\sqrt{\text{area}}}$ and $\Delta_{\sqrt{\text{area}}}$ are known from CT optimisation;
2. The systematic uncertainty is computed based on $\Delta_{\sqrt{\text{area}}}$ for each measured quantity provided by the defect detection algorithm, and correction values are corrected by subtracting this systematic uncertainty;
3. The remaining stochastic uncertainty of the corrected values is calculated;
4. The stochastic uncertainty is then propagated through all the defect characteristics derived from those measured by the defect detection algorithm.

It is helpful to recall the analytical expression for the considered defect characteristics. The expression for the sphericity, S, is:

$$S = \frac{\pi^{\frac{1}{3}}(6V)^{\frac{2}{3}}}{A}, \tag{6}$$

while the spherical equivalent diameter d_{eq} can be calculated with:

$$d_{eq} = 2\left(\frac{3V}{4\pi}\right)^{\frac{1}{3}}, \tag{7}$$

where V and A are the defect's volume and external surface area, respectively. The aspect ratio AR is defined as:

$$AR = \frac{\min\{p_x, p_y, p_z\}}{\max\{p_x, p_y, p_z\}} = \frac{m}{M}, \tag{8}$$

where p_x, p_y and p_z are the linear defect projections along the x, y, and z axes respectively. Here, m and M represent the defect's minimum and maximum axial projection.

In this case study, the set of parameters considered corresponds to a GT value equal to 130% of DGT. Since this parameter set is not optimal, a correction step is required. The expressions for the propagation of systematic uncertainties for A, V and p take the same form as those derived for stochastic uncertainties as detailed in Appendix and are presented below.

$$\Delta_A = 4(A)^{\frac{1}{2}}\Delta_{\sqrt{\text{area}}}, \tag{9}$$

$$\Delta_V = \left(\frac{4}{\sqrt{\pi}}\right)^{\frac{1}{3}}(3V)^{\frac{2}{3}}\Delta_{\sqrt{\text{area}}}, \tag{10}$$

$$\Delta_p = \frac{2}{\sqrt{\pi}}\Delta_{\sqrt{\text{area}}}. \tag{11}$$

Given the systematic uncertainty, the experimental value of a quantity can be corrected as follows:

$$Q_{corr} = Q - \Delta_Q, \tag{12}$$

where Q is the measured quantity and Q_{corr} the corrected value, free from systematic uncertainty. This correction can be applied to the measured value of A, V and p to obtain A_{corr} V_{corr}, p_{corr} respectively, and the stochastic uncertainty are computed based on the new values:

$$u_A = 4(A_{corr})^{\frac{1}{2}}u_{\sqrt{\text{area}}}, \tag{13}$$

$$u_V = \left(\frac{4}{\sqrt{\pi}}\right)^{\frac{1}{3}}(3V_{corr})^{\frac{2}{3}}u_{\sqrt{\text{area}}}, \tag{14}$$

$$u_p = \frac{2}{\sqrt{\pi}}u_{\sqrt{\text{area}}}. \tag{15}$$

$$u_S = S\sqrt{\left(\frac{u_A}{A_{corr}}\right)^2 + \left(\frac{3}{2}\frac{u_V}{V_{corr}}\right)^2}, \tag{16}$$

$$u_{d_{eq}} = \frac{2}{\sqrt{\pi}}u_{\sqrt{\text{area}}}, \tag{17}$$

$$u_{AR} = AR\sqrt{\left(\frac{u_p}{m_{corr}}\right)^2 + \left(\frac{u_p}{M_{corr}}\right)^2}. \tag{18}$$

Fig. 11 reports the results for the stochastic uncertainty of sphericity and aspect ratio. The grey dots represent defects for which the uncertainty is greater than the maximum available value for sphericity, which is theoretically one. At the same time, red dots refer to defects whose sphericity uncertainty is between the defect sphericity itself and one. Both grey and red dots indicate that the sphericity value for these defects is meaningless, as the associated uncertainty equals or even exceeds the measurement itself. Notably, these two clusters contain only small defects. Table 7 presents the cardinality of the three clusters shown in Fig. 11a.

Table 8 reports the median values of all the distributions of uncertainties related to the considered defect features. The median of these distributions can be assumed as a representative of the stochastic uncertainty of the corresponding quantity. Note that $u_{\sqrt{\text{area}}}$ and $u_{d_{eq}}$ are the same for all the defects because they do not depend on the experimental measurement. Moreover, their values are comparable with the voxel sizes adopted for the CT scans, 12x12x12 μm. The median stochastic uncertainty of S, $\overline{u_S}$, is based only on defects with uncertainty lower than the measurement. As can be seen, the median of the distribution of u_S is high due to a large number of small defects (Fig. 10), which are more sensitive to volume and external surface area measurement errors.

Table 7
Percentages of the three defect clusters classified according to the value of u_S.

Cluster	% of defects
$u_s > 1$	0.14
$S \le u_S \le 1$	9.51
$u_S < S$	90.35

Table 8
Median stochastic uncertainty for $\sqrt{\text{area}}$, equivalent diameter, sphericity and aspect ratio.

$u_{\sqrt{\text{area}}}$	$u_{d_{eq}}$	$\overline{u_S}$	$\overline{u_{AR}}$
[μm]	[μm]	[−]	[−]
11	12	0.5	0.2

3.4. Experimental defect classification

The database considered herein underwent K-means clustering to classify defects as GP, KH and LOF based on $\sqrt{\text{area}}$, sphericity, and aspect ratio. Intentionally, d_{eq} was not considered among the input features since it offers redundant information compared to $\sqrt{\text{area}}$.

The maximum number of iterations to find the optimal classification was fixed at 1000. Since each selected input feature may span different ranges, each feature was independently normalised before K-means clustering:

$$Q_{\text{norm}_2} = \frac{Q - Q_{\min}}{Q_{\max} - Q_{\min}}, \qquad Q \in \{AR, S, \sqrt{\text{area}}\}. \tag{19}$$

where Q_{norm_2}, $Q_{\min}$ and $Q_{\max}$ are the normalised, minimum and maximum values of the generic quantity Q respectively.

Following the K-means clustering, the resulting labelled samples were fed as input into an SVC algorithm with a linear kernel to determine the decision boundaries between the considered classes. In this regard, the SVC was trained on 80% of the samples randomly selected from the dataset, reserving the remainder for validation. Since a linear kernel was adopted, the SVC returned the following planar decision boundaries (in implicit form):

$$p_1 : 3.4\sqrt{\text{area}}_{\text{norm}} - 21.9\,S - 10.1\,AR + 20.0 = 0, \tag{20}$$

$$p_2 : 26.8\sqrt{\text{area}}_{\text{norm}} - 9.9\,S + 2.7\,AR - 23.6 = 0, \tag{21}$$

$$p_3 : 2.1\sqrt{\text{area}}_{\text{norm}} + 21.7\,S + 10.5\,AR - 26.1 = 0, \tag{22}$$

$p_i, i = 1,2,3$ refers to the labels in Fig. 12d. Note that Eqs. (20)–(22) refer to $\sqrt{\text{area}}_{\text{norm}}$ and not to $\sqrt{\text{area}}_{\text{norm}_2}$. Specifically, p_1 is the plane that separates the GP and LOF clusters, p_2 separates the GP and KH clusters, and p_3 separates the KH and LOF clusters.

The results of the clustering are shown in Fig. 12a-c. The graphs a, b and c of Fig. 12 were obtained with the Python library named *hexbin*, allowing us also to represent the point density with a logarithmic scale. Each cluster region is divided into hexagonal bins, and the intensity of the colour is related to the number of defects contained in the bin. Fig. 12d shows the 3D view of the entire defect database clusterised by K-Means, with the planar boundaries obtained using the SVC algorithm superimposed.

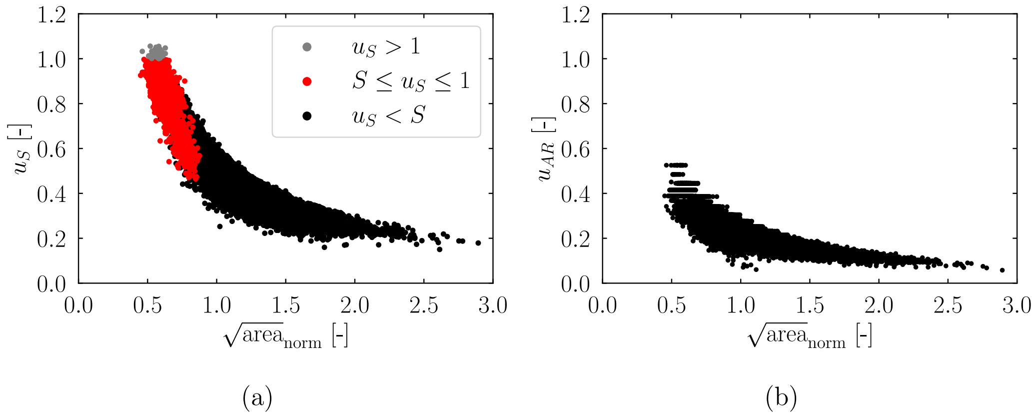

Fig. 11. Stochastic uncertainty of: (a) sphericity and (b) aspect ratio as a function of the defect $\sqrt{\text{area}}$.

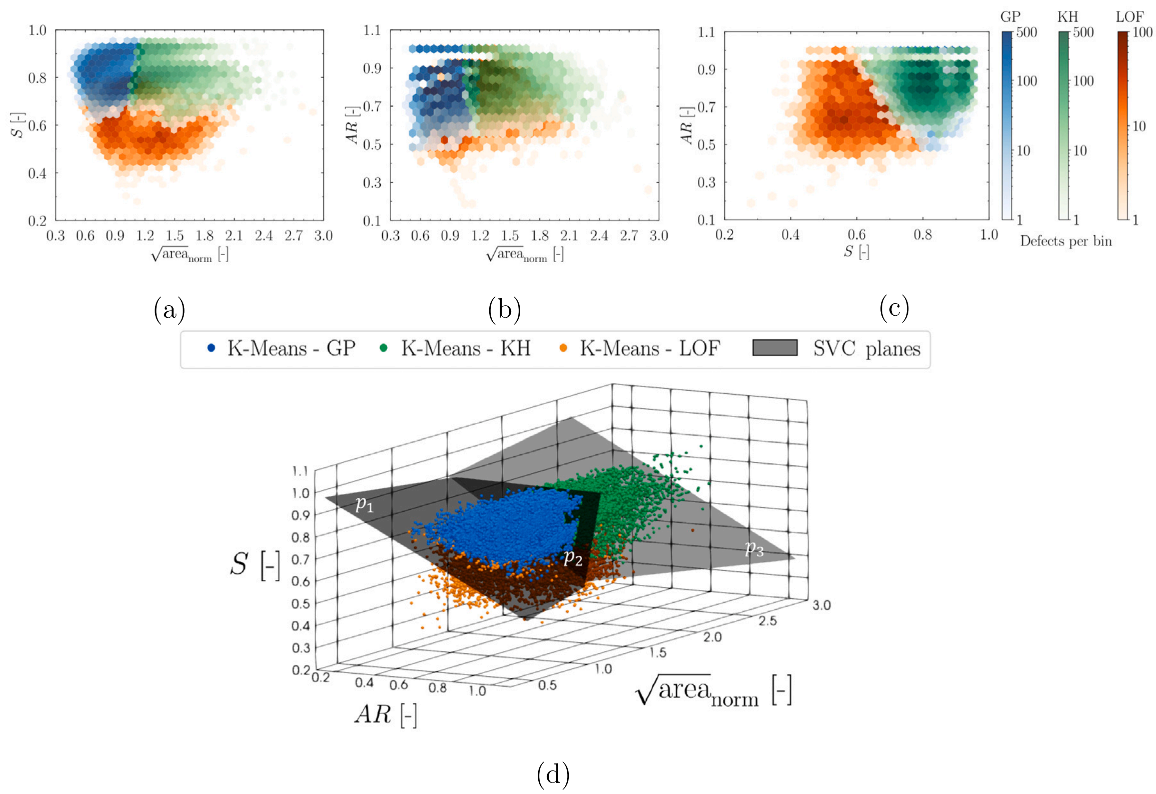

Fig. 12. Sample distributions in the features space. Each panel depicts sample coloured by the K-Means labels. (a) $\sqrt{\text{area}} - S$. (b) $\sqrt{\text{area}} - AR$. (c) $S - AR$. (d) 3D overview of the dataset along with the SVC decision boundaries (Eqs. (20)–(22)).

Fig. 13 shows the box plots of the defect characteristics grouped by defect cluster. As expected, KHs and LOFs have the greater dimensions while GPs and KHs are the most spherical and show a greater degree of shape regularity compared to LOFs.

The confusion matrix in Table 9 quantitatively compares the performance of the classification algorithms of the present study, i.e. K-Means, SVC. The diagonal entries represent the number of samples on which both classifiers agreed. The remainder of the entries are the samples that SVC classified differently from K-means. Overall, the accuracy of the SVC algorithm is 99.0% (correctly classified samples divided by the whole population). The high accuracy achieved by the SVC demonstrated the reliability of the methodology used to find analytical expressions to define defect decision boundaries, which are not provided by the K-means algorithm.

The boundaries depicted in Fig. 12d and explicited by Eqs. (20)–(22) do not aim to have a general meaning. What is proposed here is an easy way of classifying the defects, which takes into account dimensional and morphological defect characteristics. Systematic error has been removed from these characteristics, but stochastic error persists. Especially for small defects, with a $\sqrt{\text{area}}$ lower than the median value of the corresponding distribution, the stochastic uncertainty of sphericity is too high to consider the corresponding measurements truly reliable.

Table 9
Confusion matrix associated to the SVC algorithm application on the K-Means clustering.

Number of	GP_{SVC}	KH_{SVC}	LOF_{SVC}
$GP_{K\text{-Means}}$	48.90%	0.40%	0.00%
$KH_{K\text{-Means}}$	0.05%	37.70%	0.00%
$LOF_{K\text{-Means}}$	0.40%	0.15%	12.40%

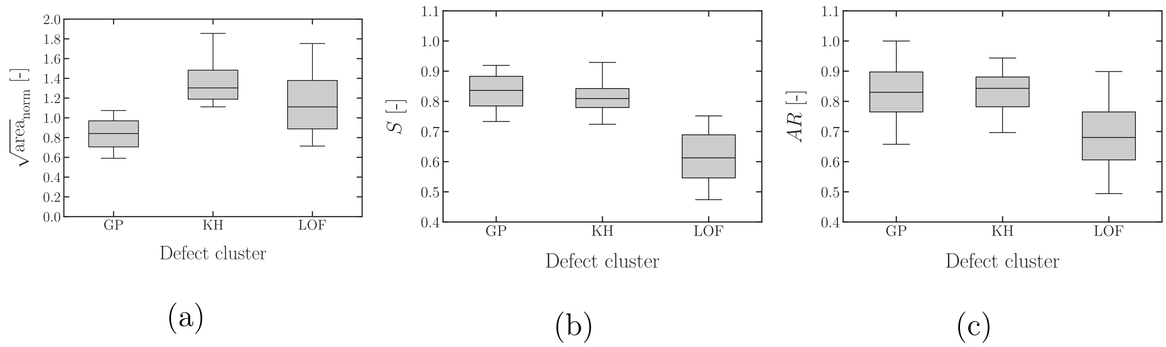

Fig. 13. Box plots of the distributions of defect characteristics: (a) $\sqrt{\text{area}}_{\text{norm}}$, (b) S and (c) AR according by defect clusters. The line inside each box represents the median of the distributions, while the edges of the box indicate the interquartile range. The whiskers extend from the 5th to the 95th percentile of the corresponding distributions.

This means that, in particular, the classification of small defects, which is based also on sphericity, is affected by a certain amount of uncertainty. However, the defects that are more detrimental to mechanical properties, especially fatigue life, are those with large dimensions. Fig. 11 shows that u_S is limited to small values for the larger defects. This allows us to reasonably suppose that defect clustering is more robust for those types of defects that are more detrimental, such as LOFs and KHs.

4. Conclusions

This study presented a procedure for optimising the parameters of CT scan defect analysis. The key aspect of the proposed methodology is that the $\sqrt{\text{area}}$ determined by fractography is used as a reference measurement to determine the difference between the actual defect size and the size measured using CT. This procedure enabled the computation and removal of the systematic error in the measurement of internal defect sizes.

The methodology was validated using 11 Ti6Al4V samples produced via electron beam melting (EBM). The grey threshold (GT) and the level of probability (POD) were selected for optimisation as they have the most significant impact on defect reconstruction. Furthermore, as the proposed methodology involves 3D reconstruction of defects, the mesh extraction algorithm (MEA) was carefully selected to minimise its impact on the defect dimensions.

Only three iterations with different GT values were needed to establish a linear relationship between the systematic error of $\sqrt{\text{area}}$ and GT. This relationship enables the extrapolation of the GT, which nullifies the systematic error (134% of the GT computed by VGstudio Max®). After analysing the data, it was also possible to select the optimal level of POD (0.5) and the best MEA (grid-based).

The propagation of uncertainty highlights that indirectly measured defect characteristics, such as sphericity, aspect ratio and equivalent diameter, may be subject to significant uncertainty. Specifically, the residual stochastic uncertainty of $\sqrt{\text{area}}$ was 11 μ m, resulting in median stochastic uncertainties of 0.5, 0.2 and 12μ m for sphericity, aspect ratio and equivalent diameter, respectively. The uncertainties of $\sqrt{\text{area}}$ and d_{eq} are comparable to the voxel sizes (12x12x12μ m). The uncertainty estimated for linear dimensions is slightly higher than that reported by Zanini et al. [36] in the measurement of lattice structures. This difference may be attributed to the greater geometric irregularity of defects, which makes segmentation more challenging and prone to variability. Improving the quality of CT scans is crucial for obtaining more accurate data to build and calibrate new fatigue models. A defect classification based only on $\sqrt{\text{area}}$, defect sphericity and aspect ratio was proposed. Implementing an SVC algorithm enables the determination of analytical expressions for the linear boundaries between K-Means-based clusters with an accuracy of 99.0%. The uncertainty associated with certain defect characteristics, such as sphericity and aspect ratio, varies with their absolute values. Therefore, the defect classification process must account for this dependency to ensure a reliable analysis.

CRediT authorship contribution statement

Emanuele Avoledo: Writing – original draft, Visualization, Methodology, Formal analysis, Data curation, Conceptualization. **Marco Petruzzi:** Writing – review & editing, Investigation, Data curation, Conceptualisation. **Marco Pelegatti:** Writing – review & editing, Validation, Methodology, Data curation. **Alessandro Tognan:** Writing – review & editing, Visualization, Methodology. **Francesco De Bona:** Writing – review & editing, Methodology. **Michele Pressacco:** Funding acquisition, Project administration, Writing – review & editing. **Riccardo Toninato:** Writing – review & editing, Conceptualization. **Enrico Salvati:** Writing – review & editing, Visualization, Supervision, Project administration, Methodology, Funding acquisition, Conceptualization.

Declaration of competing interest

The authors declare that they have no known competing financial interests or personal relationships that could have appeared to influence the work reported in this paper.

Acknowledgements

This work has been supported by the project: "NutShell - NUmerical modelling and opTimisation of SHELL Structures Against Fracture and Fatigue with Experimental Validations" funded by the MUR Progetti di Ricerca di Rilevante Interesse Nazionale (PRIN) Bando 2022, Italy – NextGenerationEU - PNRR M4.C2.1.1 - PRIN 2022 - Codice 20229BM9EL – CUP G53D23001140006; "CONCERTO – Multiscale modelling/characterisation and fabrication of nanocomposite ceramics with improved toughness" funded by the MUR Progetti di Ricerca di Rilevante Interesse Nazionale (PRIN) Bando 2020, Italy – grant 2020BN5ZW9; "POR FESR 2021–2027 - Ricerca e sviluppo - Bando 2022 - Progetto EFESTO Prat. N. 2022/76" funded by Regione FVG.

Appendix. Mathematical derivations of the uncertainties of the defect characteristics

This appendix aims to give more details on how the expressions of the uncertainties of defect characteristics were obtained. It is helpful to recall the general expression for linear error propagation. Let Q be a quantity function of $x_1, \ldots, x_n$ variables, then the related uncertainty, u_Q is:

$$u_Q = \sqrt{\left(\frac{\partial Q}{\partial x_1} u_{x_1}\right)^2 + \left(\frac{\partial Q}{\partial x_2} u_{x_2}\right)^2 + \cdots + \left(\frac{\partial Q}{\partial x_n} u_{x_n}\right)^2}, \tag{A.1}$$

where $u_{x_1}, u_{x_2}, \ldots, u_{x_n}$ represent the uncertainty associated with $x_1, x_2, \ldots, x_n$ respectively.

All the quantities involved in the uncertainty quantification in this study can be expressed as a product of terms in this way:

$$Q = c x_1^{a_1} \cdot x_2^{a_2} \cdot \ldots \cdot x_n^{a_n}, \text{ with } c, a_1, a_2, \ldots, a_n \in \mathbb{R}, \tag{A.2}$$

accordingly, Eq. (A.1) can be simplified and tailored to this specific context as follows:

$$u_Q = Q\sqrt{\left(a_1 \frac{u_{x_1}}{x_1}\right)^2 + \left(a_2 \frac{u_{x_2}}{x_2}\right)^2 + \cdots + \left(a_n \frac{u_{x_n}}{x_n}\right)^2}. \tag{A.3}$$

In this study, the quantities measured directly from the CT scans by VGEasyPore® were surface area, A, volume, V, and axial projections, p. A spherical shape was assumed for all the defects to have analytical expressions for all the defect characteristics. In particular, the expressions for surface area and volume are the following:

$$A = 4\pi r^2, \tag{A.4}$$

$$V = \frac{4}{3}\pi r^3, \tag{A.5}$$

where r is the sphere's radius, which approximates the defect's shape. Therefore, Eq. (A.1) is reduced to multiply the derivative of both the expressions by the radius uncertainty, u_r:

$$u_A = \frac{dA}{dr}u_r = 8\pi r u_r, \tag{A.6}$$

$$u_V = \frac{dV}{dr}u_r = 4\pi r^2 u_r. \tag{A.7}$$

Since a spherical shape is assumed for the defects, the corresponding axial projection is comparable with the diameter of the sphere. Therefore, the uncertainty associated with p is twice u_r:

$$u_p = 2u_r. \tag{A.8}$$

The defect analysis did not quantify the radius of the defect; however, it can be explicitly calculated using the expressions provided in Eq. (A.4)–(A.5). Moreover, one outcome of optimising CT post-processing parameters is $u_{\sqrt{\text{area}}}$, which corresponds to the only experimentally determined uncertainty among all the defect characteristics. The relationship between r and $\sqrt{\text{area}}$ provides a means to relate u_r to $u_{\sqrt{\text{area}}}$. Under the spherical defect shape assumption, the following can be stated:

$$\sqrt{\text{area}} = \sqrt{\pi r^2}, \tag{A.9}$$

hence, u_r is given by:

$$u_r = \frac{dr}{d\sqrt{\text{area}}}u_{\sqrt{\text{area}}} = \frac{u_{\sqrt{\text{area}}}}{\sqrt{\pi}}. \tag{A.10}$$

Eq. (A.10) establishes the relationship between the experimentally determined value of $u_{\sqrt{\text{area}}}$ and the uncertainties u_A, u_V and u_p. Upon replacing the radius and its uncertainty with the obtained expressions that depend solely on the measured values of A, V and $\sqrt{\text{area}}$ in Eq. (A.6)–(A.7), the result is:

$$u_A = 4(A)^{\frac{1}{2}} u_{\sqrt{\text{area}}}, \tag{A.11}$$

$$u_V = \left(\frac{4}{\sqrt{\pi}}\right)^{\frac{1}{3}} (3V)^{\frac{2}{3}} u_{\sqrt{\text{area}}}. \tag{A.12}$$

$$u_p = \frac{2}{\sqrt{\pi}} u_{\sqrt{\text{area}}} \tag{A.13}$$

These uncertainties are involved in calculating the uncertainty of the defect characteristics that depend on A, V and p, i.e. equivalent diameter, d_{eq}, sphericity, S, and aspect ratio, AR.

For clarity, the expressions of d_{eq}, S and AR are reported below:

$$S = \frac{\pi^{\frac{1}{3}}(6V)^{\frac{2}{3}}}{A}, \tag{A.14}$$

$$d_{eq} = 2\left(\frac{3V}{4\pi}\right)^{\frac{1}{3}}, \tag{A.15}$$

$$AR = \frac{\min\{p_x, p_y, p_z\}}{\max\{p_x, p_y, p_z\}} = \frac{m}{M}. \tag{A.16}$$

Finally, the expressions of the uncertainties for S, d_{eq} and AR are evaluated by apply the uncertainty propagation expressed in Eq. (A.3):

$$u_S = S\sqrt{\left(\frac{u_A}{A}\right)^2 + \left(\frac{3}{2}\frac{u_V}{V}\right)^2}, \tag{A.17}$$

$$u_{d_{eq}} = \frac{2}{\sqrt{\pi}} u_{\sqrt{\text{area}}}, \tag{A.18}$$

$$u_{AR} = AR\sqrt{\left(\frac{u_p}{m}\right)^2 + \left(\frac{u_p}{M}\right)^2}. \tag{A.19}$$

It is worth noting that there is no difference between propagating the stochastic and the systematic uncertainty, so Eq. (A.11)–(A.13), and Eq. (A.17)–(A.19) can be adapted to propagate the systematic error, $\Delta_{\sqrt{\text{area}}}$, by replacing $u_{\sqrt{\text{area}}}$ with it.

Once the systematic uncertainty is quantitatively defined, it can be subtracted from the related quantities to obtain a measure affected only by the stochastic uncertainties. In particular, given a generic quantity, Q, characterised by a known value of systematic uncertainty, Δ_Q, the corrected quantity is:

$$Q_{corr} = Q - \Delta_Q \tag{A.20}$$

References

[1] Zerbst Uwe, Madia Mauro, Klinger Christian, Bettge Dirk, Murakami Y. Defects as a root cause of fatigue failure of metallic components. i: Basic aspects. Eng Fail Anal 2019;97:777–92. http://dx.doi.org/10.1016/j.engfailanal.2019.01.055.

[2] Salvati Enrico. Evaluating fatigue onset in metallic materials: Problem, current focus and future perspectives. Int J Fatigue 2024;108487. http://dx.doi.org/10.1016/j.ijfatigue.2024.108487.

[3] Madhavadas Vaishnav, Srivastava Divyansh, Chadha Utkarsh, Raj Sakthivel Aravind, Sultan Mohamed Thariq Hameed, Shahar Farah Syazwani, et al. A review on metal additive manufacturing for intricately shaped aerospace components. CIRP J Manuf Sci Technol 2022;39:18–36. http://dx.doi.org/10.1016/j.cirpj.2022.07.005.

[4] Nyamekye Patricia, Golroudbary Saeed Rahimpour, Piili Heidi, Luukka Pasi, Kraslawski Andrzej. Impact of additive manufacturing on titanium supply chain: Case of titanium alloys in automotive and aerospace industries. Adv Ind Manuf Eng 2023;6:100112. http://dx.doi.org/10.1016/j.aime.2023.100112.

[5] Tyagi Shivank A, Manjaiah M. Additive manufacturing of titanium-based lattice structures for medical applications–a review. Bioprinting 2023;30:e00267. http://dx.doi.org/10.1016/j.bprint.2023.e00267.

[6] Plocher János, Panesar Ajit. Review on design and structural optimisation in additive manufacturing: Towards next-generation lightweight structures. Mater Des 2019;183:108164. http://dx.doi.org/10.1016/j.matdes.2019.108164.

[7] Gordon Jerard V, Narra Sneha P, Cunningham Ross W, Liu He, Chen Hangman, Suter Robert M, et al. Defect structure process maps for laser powder bed fusion additive manufacturing. Addit Manuf 2020;36:101552. http://dx.doi.org/10.1016/j.addma.2020.101552.

[8] Kruth Jean-Pierre, Froyen Ludo, Van Vaerenbergh Jonas, Mercelis Peter, Rombouts Marleen, Lauwers Bert. Selective laser melting of iron-based powder. J Mater Process Technol 2004;149(1–3):616–22. http://dx.doi.org/10.1016/j.jmatprotec.2003.11.051.

[9] Sanaei Niloofar, Fatemi Ali. Defects in additive manufactured metals and their effect on fatigue performance: A state-of-the-art review. Prog Mater Sci 2021;117:100724. http://dx.doi.org/10.1016/j.pmatsci.2020.100724.

[10] Zhang Bi, Li Yongtao, Bai Qian. Defect formation mechanisms in selective laser melting: a review. Chin J Mech Eng 2017;30:515–27. http://dx.doi.org/10.1007/s10033-017-0121-5.

[11] Martin Aiden A, Calta Nicholas P, Khairallah Saad A, Wang Jenny, Depond Phillip J, Fong Anthony Y, et al. Dynamics of pore formation during laser powder bed fusion additive manufacturing. Nat Commun 2019;10(1):1987. http://dx.doi.org/10.1038/s41467-019-10009-2.

[12] Beretta Stefano, Romano Simone. A comparison of fatigue strength sensitivity to defects for materials manufactured by am or traditional processes. Int J Fatigue 2017;94:178–91. http://dx.doi.org/10.1016/j.ijfatigue.2016.06.020.

[13] Murakami Y, Endo M. Effects of defects, inclusions and inhomogeneities on fatigue strength. Int J Fatigue 1994;16(3):163–82. http://dx.doi.org/10.1016/0142-1123(94)90001-9.

[14] Salvati Enrico, Tognan Alessandro, Laurenti Luca, Pelegatti Marco, De Bona Francesco. A defect-based physics-informed machine learning framework for fatigue finite life prediction in additive manufacturing. Mater Des 2022;222:111089. http://dx.doi.org/10.1016/j.matdes.2022.111089.
[15] Tognan Alessandro, Salvati Enrico. Probabilistic defect-based modelling of fatigue strength for incomplete datasets assisted by literature data. Int J Fatigue 2023;173:107665. http://dx.doi.org/10.1016/j.ijfatigue.2023.107665.
[16] Tognan Alessandro, Patanè Andrea, Laurenti Luca, Salvati Enrico. A bayesian defect-based physics-guided neural network model for probabilistic fatigue endurance limit evaluation. Comput Methods Appl Mech Engrg 2024;418:116521. http://dx.doi.org/10.1016/j.cma.2023.116521.
[17] Li Anyi, Baig Shaharyar, Liu Jia, Shao Shuai, Shamsaei Nima. Defect criticality analysis on fatigue life of l-pbf 17-4 ph stainless steel via machine learning. Int J Fatigue 2022;163:107018. http://dx.doi.org/10.1016/j.ijfatigue.2022.107018.
[18] Bao Hongyixi, Wu Shengchuan, Wu Zhengkai, Kang Guozheng, Peng Xin, Withers Philip J. A machine-learning fatigue life prediction approach of additively manufactured metals. Eng Fract Mech 2021;242:107508. http://dx.doi.org/10.1016/j.engfracmech.2020.107508.
[19] Avoledo E, Tognan A, Salvati E. Quantification of uncertainty in a defect-based physics-informed neural network for fatigue evaluation and insights on influencing factors. Eng Fract Mech 2023;292:109595. http://dx.doi.org/10.1016/j.engfracmech.2023.109595.
[20] Taheri Hossein, Mohammad Shoaib Mohammad Rashid Bin, Koester Lucas W, Bigelow Timothy A, Collins Peter C, Bond Leonard J. Powder-based additive manufacturing-a review of types of defects, generation mechanisms, detection, property evaluation and metrology. Int J Addit Subtractive Mater Manuf 2017;1(2):172–209. http://dx.doi.org/10.1504/IJASMM.2017.088204.
[21] Shipley Harry, McDonnell Darren, Culleton Mark, Coull R, Lupoi R, O'Donnell G, et al. Optimisation of process parameters to address fundamental challenges during selective laser melting of ti-6al-4v: A review. Int J Mach Tools Manuf 2018;128:1–20. http://dx.doi.org/10.1016/j.ijmachtools.2018.01.003.
[22] Kasperovich Galina, Haubrich Jan, Gussone Joachim, Requena Guillermo. Correlation between porosity and processing parameters in tial6v4 produced by selective laser melting. Mater Des 2016;105:160–70. http://dx.doi.org/10.1016/j.matdes.2016.05.070.
[23] Snell Robert, Tammas-Williams Sam, Chechik Lova, Lyle Alistair, Hernández-Nava Everth, Boig Charlotte, et al. Methods for rapid pore classification in metal additive manufacturing. Jom 2020;72:101–9. http://dx.doi.org/10.1007/s11837-019-03761-9.
[24] Poudel Arun, Yasin Mohammad Salman, Ye Jiafeng, Liu Jia, Vinel Aleksandr, Shao Shuai, et al. Feature-based volumetric defect classification in metal additive manufacturing. Nat Commun 2022;13(1):6369. http://dx.doi.org/10.1038/s41467-022-34122-x.
[25] Minerva G, Awd M, Tenkamp J, Walther F, Beretta S. Machine learning-assisted extreme value statistics of anomalies in alsi10mg manufactured by l-pbf for robust fatigue strength predictions. Mater Des 2023;235:112392. http://dx.doi.org/10.1016/j.matdes.2023.112392.
[26] Du Plessis Anton, Sperling Philip, Beerlink Andre, Tshabalala Lerato, Hoosain Shaik, Mathe Ntombi, et al. Standard method for microct-based additive manufacturing quality control 1: Porosity analysis. MethodsX 2018;5:1102–10a. http://dx.doi.org/10.1016/j.mex.2018.09.005.
[27] Du Plessis Anton, Yadroitsev Igor, Yadroitsava Ina, Le Roux Stephan G. X-ray microcomputed tomography in additive manufacturing: a review of the current technology and applications. 3D Print Addit Manuf 2018;5(3):227–47b. http://dx.doi.org/10.1089/3dp.2018.0060.
[28] Kalender Willi A. X-ray computed tomography. Phys Med Biol 2006;51(13):R29. http://dx.doi.org/10.1118/1.596063.
[29] Van Eijnatten Maureen, van Dijk Roelof, Dobbe Johannes, Streekstra Geert, Koivisto Juha, Wolff Jan. Ct image segmentation methods for bone used in medical additive manufacturing. Med Eng Phys 2018;51:6–16. http://dx.doi.org/10.1016/j.medengphy.2017.10.008.
[30] Senthilkumaran N, Vaithegi S. Image segmentation by using thresholding techniques for medical images. Comput Sci Eng: An Int J 2016;6(1):1–13. http://dx.doi.org/10.5121/cseij.2016.6101.
[31] Bhargavi K, Jyothi S. A survey on threshold based segmentation technique in image processing. Int J Innov Res Dev 2014;3(12):234–9, arXiv preprint arXiv:2306.06211.
[32] Lifton Joseph John. Evaluating the standard uncertainty due to the voxel size in dimensional computed tomography. Precis Eng 2023;79:245–50.
[33] Lifton JJ, Malcolm AA, McBride JW. On the uncertainty of surface determination in x-ray computed tomography for dimensional metrology. Meas Sci Technol 2015;26(3):035003. http://dx.doi.org/10.1088/0957-0233/26/3/035003.
[34] Yang Xiuyuan, Sun Wenjuan, Giusca Claudiu L. An automated surface determination approach for computed tomography. NDT & E Int 2022;131:102697. http://dx.doi.org/10.1016/j.ndteint.2022.102697.
[35] Villarraga-Gómez Herminso, Thousand Jeffery D, Smith Stuart T. Empirical approaches to uncertainty analysis of x-ray computed tomography measurements: A review with examples. Precis Eng 2020;64:249–68. http://dx.doi.org/10.1016/j.precisioneng.2020.03.004.
[36] Zanini Filippo, Carmignato Simone, Savio Enrico. Two different experimental approaches for the uncertainty determination of x-ray computed tomography dimensional measurements on lattice structures. CIRP J Manuf Sci Technol 2023;47:205–14. http://dx.doi.org/10.1016/j.cirpj.2023.10.004.
[37] Müller Pavel, Hiller Jochen, Dai Y, Andreasen JL, Hansen H Nørgaard, De Chiffre Leonardo. Estimation of measurement uncertainties in x-ray computed tomography metrology using the substitution method. CIRP J Manuf Sci Technol 2014;7(3):222–32. http://dx.doi.org/10.1016/j.cirpj.2014.04.002.
[38] Zikmund Tomáš, Šalplachta Jakub, Zatočilová Aneta, Břínek Adam, Pantělejev Libor, Štěpánek Roman, et al. Computed tomography based procedure for reproducible porosity measurement of additive manufactured samples. NDT & E Int 2019;103:111–8. http://dx.doi.org/10.1016/j.ndteint.2019.02.008.
[39] Schild Leonard, Weiser Lukas, Höger Katja, Lanza Gisela. Analyzing the error of computed tomography-based pore detection by using microscope images of matched cross-sections. Precis Eng 2023;81:192–206. http://dx.doi.org/10.1016/j.precisioneng.2023.01.013.
[40] Montgomery DC. Applied statistics and probability for engineers. 2003.
[41] ISO/IEC Guide 98-3:2008-09. Uncertainty of measurement; part 3: guide to the expression of uncertainty in measurement. Technical report, GUM; 1995.
[42] Fu Yanzhou, Downey Austin RJ, Yuan Lang, Zhang Tianyu, Pratt Avery, Balogun Yunusa. Machine learning algorithms for defect detection in metal laser-based additive manufacturing: A review. J Manuf Process 2022. http://dx.doi.org/10.1016/j.jmapro.2021.12.061.
[43] Lin Zhenqiang, Lai Yiwen, Pan Taotao, Zhang Wang, Zheng Jun, Ge Xiaohong, et al. A new method for automatic detection of defects in selective laser melting based on machine vision. Materials 2021. http://dx.doi.org/10.3390/ma14154175.
[44] ISO 5832-3:2021. Implants for surgery – metallic materials part 3: wrought titanium 6-aluminium 4-vanadium alloy. Technical report, ISO; 2021.
[45] ASTM E466-15. Standard practice for conducting force controlled constant amplitude axial fatigue tests of metallic materials. Technical report, ASTM Int.; 2021.
[46] Pyka Grzegorz, Kerckhofs Greet, Schrooten Jan, Wevers Martine. The effect of spatial micro-ct image resolution and surface complexity on the morphological 3d analysis of open porous structures. Mater Charact 2014;87:104–15. http://dx.doi.org/10.1016/j.matchar.2013.11.004.